ARTICLES

Wavelength and Metal Dependence in the Photofragmentation of a Gas-Phase Lanthanide β-Diketonate Complex

Franklin P. Ow,[†] Mary T. Berry,*[,‡] P. Stanley May,[‡] and Jeffrey I. Zink*[,†]

Department of Chemistry and Biochemistry, University of California, Los Angeles, California 90095, and Department of Chemistry, University of South Dakota, Vermillion, South Dakota 57069

Received: December 21, 2006; In Final Form: March 13, 2007

The time-of-flight mass spectra of tris(2,2,6,6-tetramethyl-3,5-heptanedionato) lanthanide(III) [or $Ln(thd)_3$ with Ln = Eu, Tb, Gd] produced by laser-induced multiphoton ionization in a supersonic expansion were studied as a function of laser excitation wavelength. Resonance-enhanced multiphoton ionization (REMPI), monitoring the Eu(I) ion signal from gas-phase $Eu(thd)_3$, was observed in three distinct visible-excitation regions, corresponding to electronic absorption transitions on neutral Eu(0) atoms. The confirmation of the presence of Eu(0) atoms in the beam supports the proposed mechanism for the production of Ln atoms through sequential dissociation of neutral thd ligands from the metal following photoexcitation into ligand-to-metal charge-transfer (LMCT) states. Evidence is also presented that the LnO^+ and $LnOH^+$ fragments observed in the mass spectrum are produced via a separate, competing fragmentation pathway. The branching ratios between the two fragmentation pathways are compared for $Ln(thd)_3$ (Ln = Eu, Tb, Gd). The ligand-dissociation pathway that produces Ln atoms appears to be more favorable in $Ln(thd)_3$ complexes with low-lying LMCT states. Finally, the observation of the $Tb_2(thd)_6^+$ dimer and its associated fragmentation pattern, as well as the presence of metal carbides, which are relevant to carbon contamination in chemical vapor deposition, is discussed.

Introduction

Photofragmentation of gas-phase metal−organic complexes and the relationship of the fragmentation patterns to the electronic structure of the complexes[1−3] have drawn much attention because of their relevance in applying wavelength optimization to laser-assisted chemical-vapor deposition (CVD).[1−8] Such studies can also lead to the rational design of new CVD precursor molecules, optimized for the clean, selective deposition of metals and metal binary and ternary compounds. In conventional thermal metal−organic CVD, activation of the precursor is provided by heating the deposition substrate. Laser-assisted CVD (LCVD) does not, in principle, require any substrate heating and allows for greater latitude in the choice of substrate material, including flexible polymer substrates.[9] LCVD also provides good spatial resolution in deposition and has been used in direct-write applications.[10,11] It has further been found valuable in the preparation of metallic nanoparticles[7,12,13] and of thin films of high purity with small grain boundaries.[14]

CVD of metals,[15−19] and, in particular, of lanthanide materials, is of interest because of the extensive application of these materials as phosphors[20−22] in LEDs and laser media and because of their potential as high-dielectric gate materials for miniaturized electronic devices.[23−25] Also, TiO_2 nanoparticles deposited by metal−organic CVD show enhanced photocatalytic activity when co-doped with lanthanides,[26] and deposited Er_2O_3 films show high corrosion resistance to liquid plutonium.[27] With widespread application of lanthanide CVD and strong potential for improvements with LCVD, a study of the photofragmentation of lanthanide-based precursor molecules and its basis in electronic structure seems timely.

We have begun to explore the wavelength-dependent photofragmentation of the lanthanide−organic CVD precursor, tris(2,2,6,6-tetramethyl-3,5-heptanedionato) lanthanide(III) [$Ln(thd)_3$]. Recently, we described a mechanism for the production of bare metal ions in the photodissociation and photoionization of $Ln(thd)_3$.[28,29] According to this mechanism, neutral thd ligands sequentially dissociate from the metal complex through photon access of LMCT states.

The dissociation of the first ligand is illustrated schematically for $Eu(thd)_3$ in Figure 1 using a single-configurational-coordinate (SCC) potential energy diagram. The computational method for creating these SCC potentials is described in ref 28 and is based on a simple point charge−point polarizability attraction and a $1/r^{12}$ repulsion. This purely ionic model is appropriate, at least at a semiquantitative level, for lanthanide complexes, where covalent interactions with the shielded valence electrons are very weak. In this model, excitation to the repulsive wall of the LMCT state results in reduction of the metal from Eu(III) to Eu(II) and dissociation of the neutral ligand radical. Each subsequent ligand dissociation is likewise accompanied by metal reduction. The bare metal atom, Ln(0), is produced after the third ligand dissociates, and the observed ions are then formed

* To whom correspondence should be addressed. E-mail: zink@chem.ucla.edu (J.I.Z.), mberry@usd.edu (M.T.B.). Phone: (310) 825-8651 (J.I.Z.), (605) 677-5487 (M.T.B.). Fax: (310) 206-4038 (J.I.Z.), (605) 677-6397 (M.T.B.).

[†] University of California, Los Angeles.

[‡] University of South Dakota.

10.1021/jp068838h CCC: $37.00
Published on Web 05/02/2007

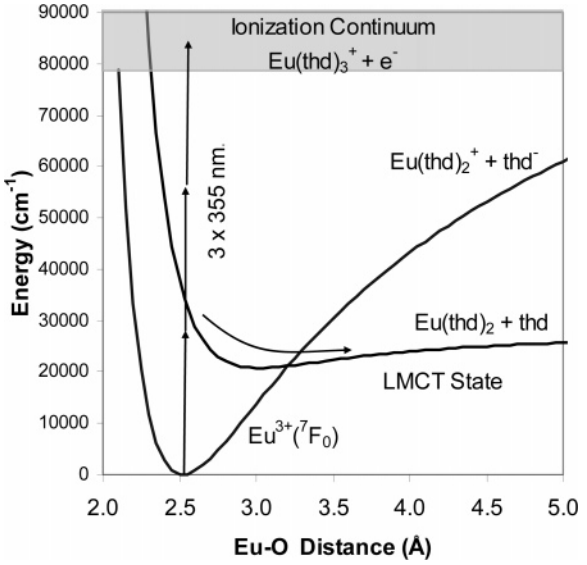

Figure 1. Potential energy diagram for $Eu(thd)_3$, showing multiphoton ionization of the intact molecule in competition with dissociation through the LMCT state into the neutral fragments $Eu(thd)_2$ and thd.

by photoionization of the atomic species. The bare metal ions are detected by mass spectrometry only upon photoionization of the neutral atomic species. Sequential ligand dissociation is supported by the observation of $Ln(thd)^+$, $Ln(thd)_2^+$, and $Ln(thd)_3^+$ fragments in the 430-nm photoionization mass spectrum for $Ln(thd)_3$ (Ln = Eu, Tb, Gd). This is illustrated in the 430-nm photoionization mass spectrum for $Eu(thd)_3$ shown in Figure 2. The proposed model is also consistent with the previous observation of atomic metal luminescence following photofragmentation of both lanthanide−organic[30] and transition metal−organic[16−18,31−34] compounds.

At a similar fluence, but using shorter-wavelength excitation (10^8 W/cm^2, 355 nm), the $Ln(thd)_n^+$ fragments are only weakly observed in the mass spectrum, which is, in this case, dominated by bare metal ions and metal oxide. This wavelength dependence can be interpreted as arising from highly efficient ligand stripping at 355 nm, with which direct multiphoton ionization of the parent and neutral $Ln(thd)_n$ intermediates cannot effectively compete.

In this article, we report the signature of atomic europium, Eu(0), in the REMPI spectrum of $Eu(thd)_3$. We also describe the variation in branching ratios of bare metal ion vs metal oxide from $Eu(thd)_3$, $Gd(thd)_3$, and $Tb(thd)_3$. We report the observation of the $Tb_2(thd)_6^+$ dimer and its associated fragmentation pattern, as well as the presence of metal carbides, which can result in carbon contamination of deposited materials. We suggest that the charge-transfer states play the dominant role in determining the photochemistry of the $Ln(thd)_3$ series and that it seems probable that analogous mechanisms are relevant to photofragmentation in a broad set of gas-phase metal−organic complexes.

Experimental Section

$Ln(thd)_3$ was purchased from Aldrich and used without further purification. The ion signal for H_2O^+ during the initial heating process demonstrated the presence of water in the original sample. All spectra reported in this work were obtained after the H_2O^+ ion signal had dissipated.

Photoionization mass spectra for each of the three samples, $Eu(thd)_3$, $Tb(thd)_3$, and $Gd(thd)_3$, were measured at 355 nm (20−65 mJ/pulse) and over the range 410−610 nm (20 mJ/pulse). The time-of-flight (TOF) mass spectrometer was constructed

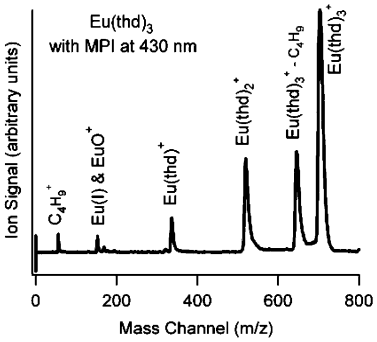

Figure 2. Multiphoton fragmentation and ionization of $Eu(thd)_3$ at 430 nm and low fluence (10^8 W/cm^2) showing strong signals for the parent ion and for species resulting from loss of entire ligands from the complex. The parent ion also exhibits a satellite feature representing loss of a *tert*-butyl group from an attached ligand.

based on a design in the literature.[35] Photoionization occurs in a stainless steel cube (30-cm edges) equipped with quartz windows and evacuated to $<10^{-6}$ Torr by a 6-in. diffusion pump fitted with a water-cooled baffle. $Ln(thd)_3$ was sublimed from a sample holder at 110−140 °C and mixed with He behind a high-speed solenoid valve (General Valve series-9, 0.5-mm orifice) with a backing pressure of about 10^3 Torr. The high-speed solenoid valve produces a 0.2-ms pulse of the sample gas whose path intersects the ionization laser beam at 90°. An OPOTEK optical parametric oscillator (410−680 nm, 6-ns pulse width, ~20 mJ/pulse, 10−20 cm^{-1} bandwidth) pumped by the third harmonic of a Quantel Brilliant Nd:YAG laser was used for excitation. An optional KV-389 filter was used to eliminate residual pump (355 nm) from the visible laser beam. Alternatively, the third harmonic of the Nd:YAG itself was used for ionization. The fragment ions were accelerated through a 1-m flight tube maintained at 10^{-6} Torr by a Varian V300HT 6-in. air-cooled turbomolecular pump. Accelerator voltages were 3000 V, 2100 V, and ground, respectively, in order from farthest to nearest the detector. Ions were detected using a 40-mm-diameter triple microchannel plate detector assembly (R. M. Jordan, Inc.). The ion signal was processed using a Tektronix TDS2022 200-MHz dual-channel digital oscilloscope interfaced to a PC.

One spectrum was obtained using 266-nm photoionization (fourth harmonic of a Nd:YAG) and a quadrupole mass spectrometer. In this case, the source molecular beam was skimmed, the sample/laser intersection was at 180°, and the carrier gas was Ar.

The REMPI spectrum for $Eu(thd)_3$ was measured with the TOF system described above. The integrated Eu(I) ion signal was referenced to the EuO^+ signal. This latter species showed little wavelength dependence over the range of interest, and thus, the ratio could be used to mitigate the effects of shot-to-shot fluctuations in laser power and sample delivery. The ion-signal ratio $Eu(I)/EuO^+$ was measured as a function of photoionization wavelength to identify possible Eu(0) resonances in the spectrum and otherwise characterize the source of the Eu(I) ions.

For a qualitative comparison, single-configurational-coordinate (SCC) potential energy curves were calculated for the $Ln(thd)_{1-3}$ complexes and for the excited charge transfer states using a simple point charge−point polarizability method described in detail in ref 28.

Results and Discussion

Figure 3 shows the 455−470-nm REMPI spectrum of $Eu(thd)_3$, monitoring the integrated Eu(I) ion signal. The peaks in Figure 3 are attributed to resonance enhancement through $^8S_{7/2}$

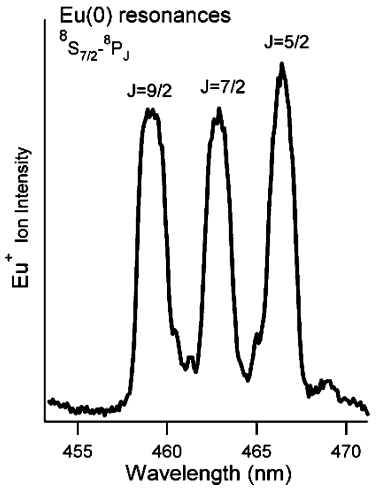

Figure 3. Photoionization of Eu(thd)$_3$ showing resonance enhancement of the Eu(I) ion signal as a function of photoionization wavelength. The peaks correspond to a Eu(0) s → p atomic transition. The spin−orbit splitting of the ^8P_J state is evident. At peak maxima, the Eu(I) enhancement is approximately 4-fold.

→ ^8P_J ($J = {}^5/_2, {}^7/_2, {}^9/_2$) absorbance from the atomic ground state of Eu(0) ([Xe]6s^{2}4f^7).[36] In measuring this spectrum, residual 355-nm light from the Nd:YAG pump was not filtered from the photoionization beam. Interestingly, the Eu(I) ion signal was very weak when the residual 355-nm light was filtered from the visible excitation beam. A reasonable interpretation is that the 355-nm excitation is important in forming the Eu(0) atoms in good yield, and their subsequent photoionization to Eu(I) is enhanced by resonance absorption via the Eu(0): $^8S_{7/2} \rightarrow {}^8P_J$ transition in the 455−470-nm region. Enhancement in the Eu(I) signal was also observed at wavelengths of 565 and 602 nm, which match additional Eu(0): $^8S_{7/2} \rightarrow {}^6P_{5/2}$ and Eu(0): $^8S_{7/2} \rightarrow {}^8P_{9/2}$ transitions, respectively. The REMPI data strongly support the presence of neutral Eu(0) atoms in the beam, lending further support to our proposed photoionization/photofragmentation mechanism (see Introduction).

In addition to the sequential ligand-dissociation pathway, which leads to the production of neutral metal atoms, a separate, distinct mechanistic pathway produces LnO^+ and $LnOH^+$ in significant yield using 355-nm, 266-nm, and to a lesser extent visible photoionization. At high fluence, these species apparently undergo further fragmentation and photoionization, yielding Ln(II) and Ln(III). Schematically, the sequential ligand-dissociation mechanism

$$\mathrm{Ln(thd)_3} \rightarrow \mathrm{Ln(thd)_2} \rightarrow \mathrm{Ln(thd)} \rightarrow \mathrm{Ln(0)} \rightarrow \mathrm{Ln(I)} \rightarrow \mathrm{Ln(II)} \rightarrow \mathrm{Ln(III)} \quad \text{(I)}$$

is in competition with a second pathway represented by

$$\mathrm{Ln(thd)_3} \rightarrow\rightarrow \mathrm{LnO^+, LnOH^+} \rightarrow\rightarrow \mathrm{Ln(II)} \rightarrow \mathrm{Ln(III)} \quad \text{(II)}$$

These two distinct mechanistic pathways appear common to all three metals, but the branching ratios between them differ for Eu, Gd, and Tb. At low laser fluence (~10^8 W/cm^2), pathways I and II can be terminated at Ln(I) or at LnO^+, $LnOH^+$, respectively, with essentially no production of Ln(II) or Ln(III).

The branching ratios between pathways I and II for all three Ln(thd)$_3$ complexes were compared by measuring the Ln(I)/(LnO^+, $LnOH^+$) ion-signal ratio for each sample. For these measurements, laser fluence was lowered until no Ln(II) or Ln(III) ion signal was observed. Measurements were made at 355 nm and in the range of 420−440 nm. Outside the 420−440-nm range, the metal and metal oxide ion signals were generally weak because of low laser power on the short-wavelength side and poor ionization efficiency on the long-wavelength side [with the exceptions noted earlier for the REMPI of Eu(thd)$_3$ at 565 and 602 nm].

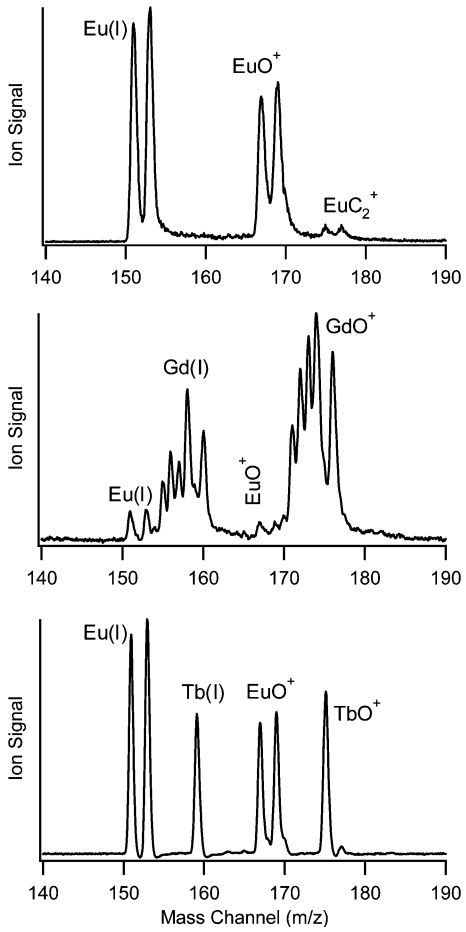

Figure 4. Photoionization of Ln(thd)$_3$ at 355 nm and low fluence (~10^8 W/cm^2). The Ln(II) signal at this fluence is small. At higher fluence, both Ln(I) and LnO^+ are converted to Ln(II). The differences in the Ln(I)-to-LnO^+ ion-signal ratio reflect the relative accessibility of the LMCT state for the three metals.

The relevant regions of the low-fluence 355-nm photoionization mass spectra are shown in Figure 4. The Eu(I) ion signal is greater than that from EuO^+, whereas for Tb(thd)$_3$ and Gd(thd)$_3$, the LnO^+ ion signal is greater than that from Ln(I). The $LnOH^+$ signal is apparent only at 266 nm. The Ln(I)/LnO^+ ion-signal ratio, and, therefore, the tendency to favor pathway I over pathway II, increases in the order Gd(thd)$_3$ < Tb(thd)$_3$ < Eu(thd)$_3$. Likewise, throughout the 420−440-nm region, the Ln(I)/LnO^+ ratio is greatest for Eu(thd)$_3$ and smaller for Tb(thd)$_3$ and Gd(thd)$_3$.

Our proposed model for the sequential ligand-dissociation mechanism (pathway I) involves successive excitations into the LMCT state of the Ln(thd)$_n$ complex, resulting in reduction of the Ln metal ion and dissociation of the neutral ligand radical, and leading ultimately to bare Ln(0) atoms. This model is illustrated with SCC potential energy curves in Figure 5 for Eu(thd)$_3$ (top), Gd(thd)$_3$ (middle), and Tb(thd)$_3$ (bottom). Each panel in Figure 5 shows two potential energy curves: one for the Ln(thd)$_n$ ground state and one representing the LMCT state.

Not surprisingly, the LMCT state always has a greater equilibrium bond distance than does the ground state, because

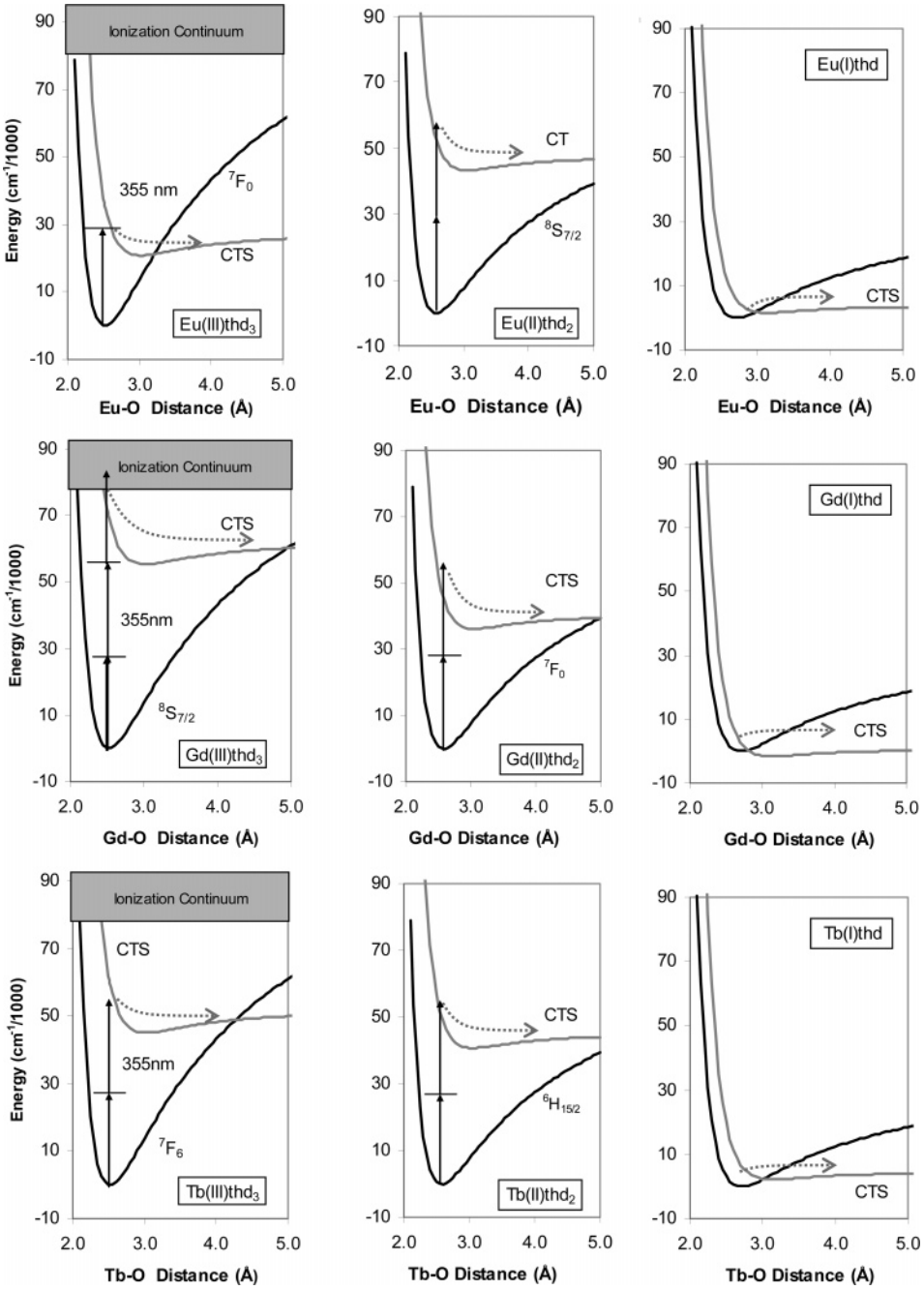

Figure 5. Single-configurational coordinate (SCC) potential energy diagrams for $Ln(thd)_n$ showing the ground electronic state that correlates with the ionic species $Ln(thd)_{n-1}^+ + thd^-$ and the excited LMCT state that correlates with the neutral fragments $Ln(thd)_{n-1} + thd$. Vertical arrows represent absorbance of 355-nm photons. Vertical optical transitions to the LMCT are predicted to result in formation of the complex on the repulsive wall and above the dissociation limit of the LMCT, resulting in dissociation of the intact (neutral) ligand fragment. This dissociation is illustrated by the curved dashed-line arrows. The first panel in each row illustrates dissociation of the parent $Ln(thd)_3$ into products $Ln(thd)_2 + thd$. The second panel illustrates the dissociation of that $Ln(thd)_2$ product, yielding $Ln(thd) + thd$. The third panel then illustrates the dissociation of the monoligated Ln(thd), yielding the bare metal atom, Ln(0), and the netral thd ligand radical. The greatest difference between the three metals in the energies of the LMCT occurs for the first dissociation step (first panel).

the neutral thd ligand shows a weaker attraction for the metal than does the ligand anion of the ground state. Thus, Franck−Condon overlap between the ground state and the excited LMCT state is maximized on the repulsive wall of the LMCT and, in most cases, at energies above the dissociation limit of the weakly bound state. Excitation into the LMCT, therefore, is predicted to result in dissociation of the intact neutral ligand.

Referring to the leftmost panels in Figure 5, the LMCT state of the $Ln(thd)_3$ complex consists of a neutral ligand radical and two negatively charged ligands bound to Ln(II). The energy of this first LMCT state is directly related to the third ionization potential of Ln [i.e., the energy difference between the charge-transfer Ln(II) and the ground-state Ln(III)] and to the electron affinity of the thd^- ligand anion. A high ionization potential for Ln(II) stabilizes the LMCT state relative to the ground state. Because Eu(II) has a stable, half-filled-shell electron configuration, $[Xe]4f^7$, the LMCT for $Eu(thd)_3$ lies significantly lower in energy (3−4 eV) than the analogous states in $Gd(thd)_3$ or $Tb(thd)_3$. This follows directly from the Eu(II) ionization potential, which is higher than those for Gd(II) and Tb(II) by

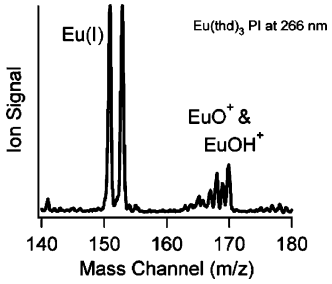

Figure 6. Photoionization of $Eu(thd)_3$ at 266 nm and low fluence ($\sim 10^7$ W/cm^2) resulting in no detectable Eu(II) signal. The Eu(I) ion signal exceeds the integrated oxide ion signal by a factor of 3:1.

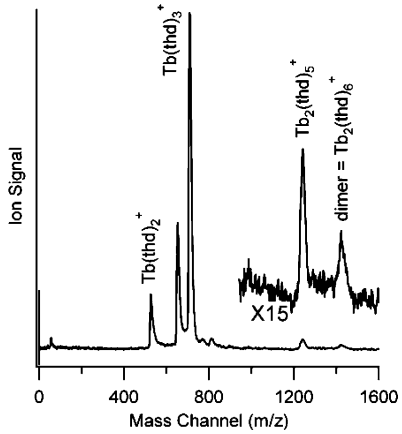

Figure 7. Photoionization mass spectrum of $Tb(thd)_3$ at 430 nm ($\sim 10^8$ W/cm^2) showing evidence of a gas-phase binuclear complex.

TABLE 1: Ratio of Integrated Ion Signals, Ln(I)/(LnO^+, $LnOH^+$), for Low-Fluence (10^7-10^8 W/cm^2) Photoionization of $Ln(thd)_3$

λ (nm)	Eu	Gd	Tb
266	3.2	–	–
355	1.3	0.49	0.81
430	2.2	0.87	0.65

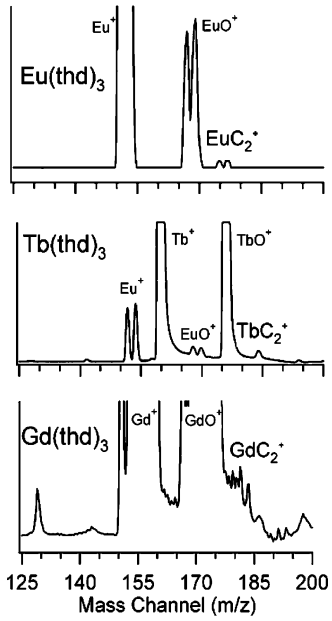

Figure 8. Photoionization mass spectra of $Ln(thd)_3$ at 355 nm ($\sim 10^9$ W/cm^2) showing minor features attributable to the metal carbide that might result in carbon contamination of deposited films.

4.3 and 3.0 eV, respectively. The relatively low energy (easy access) of the first LMCT in $Eu(thd)_3$ promotes the basic ligand-stripping mechanism at the expense of oxide production, ultimately increasing the branching ratio, Eu(I)/(EuO^+, $EuOH^+$). At 266 nm, in closer resonance with the $Eu(thd)_3$ LMCT,[37] the ratio is further increased as illustrated in Figure 6.

Referring to the middle and rightmost panels in Figure 5, the positions of the LMCT for the second and third ligand-dissociation steps involve Ln(II) → Ln(I) in the bis complex, $Ln(thd)_2$, and Ln(I) → Ln(0) in the monoligated Ln(thd), respectively. The energies of the LMCT are, therefore, related to the second and *first* Ln ionization potentials, which are more similar across the Eu−Gd−Tb series than are the third ionization potentials. Consequently, the second and third dissociation steps have a smaller impact on the relative metal-to-oxide branching ratios across the Eu−Gd−Tb series.

In summary, we suggest that the observed trend in the relative tendency toward pathway I is governed mainly by the efficiency of the first ligand-dissociation step, which, in turn, is favored by a low-lying LMCT on $Ln(thd)_3$. We note, however, that, as the wavelength is increased from 355 nm, LMCT excitation of $Tb(thd)_2$ switches from a two- to a three-photon process before $Gd(thd)_2$, which might explain the reversal in the relative branching ratios between Gd and Tb at 430 nm as compared to 355 nm. The branching ratios, derived from integrated ion intensities, are summarized in Table 1.

For all three metals, the third dissociation step (third panel of Figure 5), Ln(thd) → Ln(0) + thd, is predicted to require very little energy. For this calculation, as in ref 28, the electron affinity of the thd^- ligand anion was assigned as 1 eV. If that assignment were increased, the barrier to dissociation would be increased as well. Nevertheless, it is predicted that this last step is at most a one-photon process in the visible and UV regions and might indeed proceed thermally in a zero-photon process. It is interesting to note that Eu(thd), which, of the three metals, shows the highest barrier to dissociation, is the only monoligated complex represented in the corresponding 430-nm photoionization mass spectra (see Figure 2). $Tb(thd)^+$ and $Gd(thd)^+$ are not observed in the corresponding $Tb(thd)_3$ and $Gd(thd)_3$ spectra.[29]

Figure 7 shows the photoionization mass spectrum of $Tb(thd)_3$ at 430 nm. The $Tb_2(thd)_6^+$ dimer is observed, as well as a fragment with *m*/*z* corresponding to $Tb_2(thd)_5^+$. The $Ln(thd)_3$ crystal structure for the lighter lanthanides, through dysprosium and, thus, including terbium, contains a binuclear molecular complex with the two metal ions bridged by a pair of ligands.[38,39] In dilute *n*-hexane solution[40] and in the gas phase[41] at elevated temperatures, the structure is thought to be predominantly mononuclear. Whether the gas-phase binuclear complex reported here sublimed with this structure or was formed in the supersonic expansion from condensation of monomers is unclear. However, the observed $Tb_2(thd)_6$ complex does appear to be more stable than a simple van der Waals cluster, as the metal pairing is robust against direct multiphoton ionization and single-ligand loss.

In previous work,[37] it was noted that charge-transfer quenching of the $^5D_0$ electronic state of Eu(III) was some 40 times more effective in the binuclear crystalline system than in the predominantly monomeric solution and gas-phase species. It is interesting to speculate as to whether this suggests that the most likely charge transfer is from one of the two bridging ligands and whether this explains why the binuclear complex is stable to loss of one, but not two, ligands. It is also interesting to consider the electronic structure of the presumed-neutral Tb_2-

$(thd)_5$ species, from which the observed $Tb_2(thd)_5^+$ is thought to arise. To what extent is this binuclear complex stabilized by the Tb(II)−Tb(III) mixed valence? In future work, we will search for the existence of the gas-phase $Ln_2(thd)_6$ dimer of other lanthanides and attempt to measure their dependence on sublimation temperature and backing pressure of the expansion. It is quite likely that the absence of the $Eu_2(thd)_6$ and $Gd_2(thd)_6$ dimers in the reported spectra is related to optimization conditions in the mass spectrometer and molecular beam and is not indicative of unfavorable formation. Future measurements of dimer dependence on experimental conditions should reveal whether the species sublimed as a dimer or formed from monomers in the expansion, perhaps first as a van der Waals complex that subsequently rearranged to the stable bridged structure.

Also observed for all three metals at 355 nm are weak ion signals due to the metal carbides, LnC^+ and LnC_2^+, with the latter being the stronger of the two, as illustrated in Figure 8. These features are even stronger in the mass spectrum of $Eu(thd)_3$ at 266 nm shown in Figure 6. The carbides are relevant to potential carbon contamination in CVD.[1,16,18,19,31] Future work will consider strategies for carbide elimination through laser wavelength and power selection.

Conclusion

Photoionization mass spectrometry and REMPI of $Ln(thd)_3$ (Ln = Eu, Gd, and Tb) with low-fluence visible irradiation reveal the mechanism for production of the bare metal through a series of metal-reduction/ligand-dissociation steps yielding atomic Ln(0). This mechanism depends on photon access of LMCT states and is, therefore, sensitive to the nature of the metal and its first three ionization potentials. Differences in the efficiency of this mechanism for the three $Ln(thd)_3$ are thought to arise mainly in the first ligand-dissociation step.

In competition with this ligand-stripping process is a mechanism for production of the metal oxide. The relatively low energy (easy access) of the first LMCT in $Eu(thd)_3$ promotes the ligand-stripping mechanism at the expense of oxide production, resulting in the highest metal-to-oxide branching ratio for europium. Photochemical carbide production is also observed for all three metals and is a potential source of carbon contamination for LCVD films and nanoparticles.

This work provides significant insight into the photochemistry of gas-phase lanthanide−organic complexes and has the ultimate aim of addressing the following questions: If LCVD is to reach its full potential for clean selective deposition of materials, will it then be possible to use wavelength-dependent photofragmentation to optimize production of the bare metal by tuning into resonance with the LMCT or conversely to optimize production of the oxide or other binary compounds by avoiding the LMCT? Will it be possible to simultaneously choose a wavelength to minimize production of carbide or other potential contaminants? Future studies are warranted on potential single-source precursors for deposition of nitrides and sulfides and for differently substituted β-diketonates with shifted LMCT states.

Acknowledgment. This work was made possible by a grant from the National Science Foundation to J.I.Z. (CHE-0507929). Acknowledgment is also made to the donors of the American Chemical Society Petroleum Research Fund for partial support of this research (M.T.B. and P.S.M.).

References and Notes

(1) Muraoka, P.; Byun, D.; Zink, J. I. *Coord. Chem. Rev.* **2000**, *208*, 193−211.

(2) Byun, D.; Zink, J. I. *Inorg. Chem.* **2003**, *42* (14), 4308−4315.

(3) Muraoka, P.; Byun, D.; Zink, J. I. *J. Phys. Chem. A* **2001**, *105* (38), 8665−8671.

(4) Yamazaki, Y.; Hioki, T.; Funakubo, H.; Shinozaki, K.; Mizutani, N. *Mater. Res. Bull.* **1995**, *30*, 1081−1088.

(5) Ouchi, A.; Bastl, Z.; Bohacek, J.; Orita, H.; Miyazaki, K.; Miyashita, S.; Bezdicka, P.; Pola, J. *Chem. Mater.* **2004**, *16*, 3439−3445.

(6) Lancoka, J.; Santonib, T. A.; Penzac, M.; Loretib, S.; Menicuccib, I.; Minarinid, C.; Jelinek, M. *Surf. Coat. Technol.* **2005**, *200*, 1057−1060.

(7) Landstrom, L.; Lu, J.; Heszler, P. *J. Phys. Chem. B* **2003**, *107*, 11615−11621.

(8) Yoshida, S.; Kikawa, J.; Itoh, Y. *J. Cryst. Growth* **2002**, *237*−*239*, 1037.

(9) Wagner-Halary, E.; Wagner, F.; Hoffman, P. *J. Electrochem. Soc.* **2004**, *151* (9), C571−C576.

(10) Boutros, K. S.; Roberts, J. C.; Bedair, S. M. *Appl. Phys. Lett.* **1996**, *68* (15), 2041−2042.

(11) Han, S. I.; Jeong, S. H. *J. Laser Appl.* **2004**, *16* (3), 154−159.

(12) Heszler, P.; Elihn, K.; Landstrom, L.; Boman, M. *J. Phys. Chem. B* **2003**, *107* (42), 11615−11621.

(13) Cheon, J.; Guile, M.; Muraoka, P.; Zink, J. I. *Inorg. Chem.* **1999**, *38* (9), 2238−2239.

(14) Cheon, J.; Talaga, D. S.; Zink, J. I. *J. Am. Chem. Soc.* **1997**, *119* (1), 163−168.

(15) Cheon, J.; Kang, H.-K.; Zink, J. I. *Coord. Chem. Rev.* **2000**, *200*−*202*, 1009−1032.

(16) Bitner, T. W.; Zink, J. I. *Inorg. Chem.* **2002**, *41* (4), 967−972.

(17) Cheon, J.; Zink, J. I. *Inorg. Chem.* **2000**, *39* (3), 433−436.

(18) Cheon, J.; Muraoka, P.; Zink, J. I. *Chem. Mater.* **2000**, *12* (2), 511−516.

(19) Muraoka, P.; Byun, D.; Zink, J. I. *J. Am. Chem. Soc.* **2000**, *122* (6), 1227−1228.

(20) (a) Steckl, A. J.; Birkhahn, R. *Appl. Phys. Lett.* **1998**, *73* (12), 1700−1702. (b) Birkhahn, R.; Hudgins, R.; Lee, D.; Steckl, A. J.; Molnar, R. J.; Saleh, A.; Zavada, J. M. *J. Vac. Sci. Technol. B* **1999**, *17* (3), 1195−1199. (c) See also: *Laser Focus World*, Feb 2005.

(21) MacKenzie, J. D.; Abernathy, C. R.; Pearton, S. J.; Hommerich, U.; Wu, X.; Schwartz, R. N.; Wilson, R. G.; Zavada, J. M. *J. Cryst. Growth* **1997**, *175*−*176* (Part 1), 84−88.

(22) Sivakumar, S.; van Veggel, F. C. J. M.; Raudsepp, M. *J. Am. Chem Soc.* **2005**, *127* (36), 12464−12465.

(23) Gordon, R. G.; Becker, J.; Hausmann, D.; Suh, S. *Chem. Mater.* **2001**, *13*, 2463−2464.

(24) Leskela, M.; Ritala, M. *J. Solid State Chem.* **2003**, *171* (1−2), 170−174.

(25) Jones, A. C.; Aspinall, H. C.; Chalker, P. R.; Potter, R. J.; Kaupo, K.; Rahtu, A.; Ritala, M.; Leskel, M. *Mater. Sci. Eng. B* **2005**, *118*, 97−104.

(26) Li, W.; Shah, S. I.; Huang, C.-P.; Jung, O.; Ni, C. *Mater. Sci. Eng. B* **2002**, *96*, 247−253.

(27) Hubbard, K. M.; Espinoza, B. F. *Thin Solid Films* **2000**, *366*, 175−180.

(28) Nelson, B. N.; Caster, A. G.; Berry, M. T. *Chem. Phys. Lett.* **2004**, *396*, 256−260.

(29) Ow, F. P.; Berry, M. T.; May, P. S.; Zink, J. I. *J. Phys. Chem. A* **2006**, *110*, 7751−7754.

(30) Campbell, M. L. *J. Phys. Chem. A* **1999**, *103* (36), 7274−7279.

(31) Talaga, D. S.; Hanna, S. D.; Zink, J. I. *Inorg. Chem.* **1998**, *37* (12), 2880−2887.

(32) Talaga, D. S.; Zink, J. I. *Inorg. Chem.* **1996**, *35* (17), 5050−5054.

(33) Cheon, J.; Zink, J. I. *J. Am. Chem. Soc.* **1997**, *119* (16), 3838−3839.

(34) Cheon, J.; Talaga, D. S.; Zink, J. I. *Chem. Mater.* **1997**, *9* (5), 1208−1212.

(35) Wiley, W. C.; McLaren, I. H. *Rev. Sci. Instrum.* **1955**, *26*, 1150−1157.

(36) Martin, W. C.; Zalubas, R.; Hagan, L. *Atomic Energy Levels—The Rare Earth Elements*; National Bureau of Standards: Washington, DC, 1978; pp 185−208.

(37) Berry, M. T.; May, P. S.; Xu, H. *J. Phys. Chem.* **1996**, *100* (22), 9216−9222.

(38) Cunningham, J. A.; Sievers, R. E. *Inorg. Chem.* **1980**, *19* (3), 595−604.

(39) Erasmus, C. S.; Boeyens, J. C. A. *Acta. Crystallogr. B* **1970**, *26* (11), 1843−1854.

(40) Desreux, J. F.; Fox, L. E.; Reilly, C. N. *Anal. Chem.* **1972**, *44* (13), 2217−2219.

(41) Sicre, J. E.; Dubois, J. T.; Eisentraut, K. J.; Sievers, R. E. *J. Am. Chem. Soc.* **1969**, *91* (13), 3476−3481.